ORIGINAL ARTICLE

lajss.org Latin American Journal of Solids and Structures

www.lajss.org

Buckling analysis of heavy tapered bi-material composite columns with elliptical cross-section

Byoung Koo Lee [a], Sang Jin Oh [b], Joon Kyu Lee [c*]

[a] Department of Civil and Environmental Engineering, Wonkwang University, 460 Iksan-daero, Iksan-si, Jellabuk-do, 54538, Korea. Email: bkleest@wku.ac.kr
[b] Department of Civil and Environmental Engineering, Jeonnam State University, 152 Jookrokwon-ro, Damyang-eup, Jellanam-do, 57337, Korea. Email: sjoh@dorip.ac.kr
[c] Department of Civil Engineering, University of Seoul, 163 Seoulsiripdae-ro, Dongdaemun-gu, Seoul, 02504, Korea. Email: jkleegeo@uos.ac.kr

* Corresponding author

https://doi.org/10.1590/1679-7825/e8837

Abstract

This study presents a detailed investigation into the stiffness characteristics and buckling behavior of heavy, tapered bi-material composite columns with the elliptical cross-section. These columns are laterally laminated using two distinct hybrid materials. The study addresses two primary objectives: (1) deriving explicit expressions for flexural rigidity and mass per unit length, and (2) applying these formulations to evaluate buckling behavior under self-weight conditions. The taper is represented by a linear variation along the bending axis of the elliptical cross-section. A governing differential equation for the buckled mode shape is formulated, and numerical techniques are applied to determine critical buckling loads and corresponding mode shapes. Parametric studies illustrate the influence of geometric and material variations, with the results presented through tables and figures.

Keywords

Buckling load, Bi-material composite, Heavy column, Tapered column, Self-weight, Elliptical cross-section.

Graphical Abstract

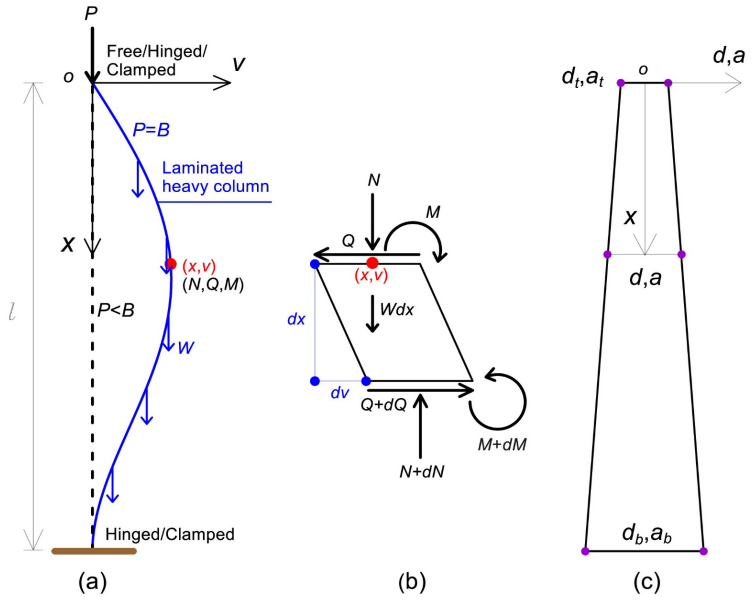

Received September 18, 2025. In revised form December 14, 2025. Accepted December 18, 2025. Available online December 24, 2025.
https://doi.org/10.1590/1679-7825/e8837

1 INTRODUCTION

Composite layered structures are widely recognized for their superior rigidity-to-weight and strength-to-weight ratios when compared to conventional metallic counterparts. These advantages enable enhanced mechanical performance without sacrificing structural integrity. As a result, the use of hybrid, multi-layered component has expanded significantly across various engineering fields. A notable example is the bi-material column, a laterally stepped material (LSM) structure characterized by abrupt changes in material properties across the cross-sectional depth.

Due to their advantageous mechanical properties, including those found in bi-material and hybrid structures, LSM configurations have received significant research attention. Numerous studies have addressed their flexural behavior, including buckling, which is central to this work. Several notable investigations exemplify key developments in the flexural analysis of such members. For instance, Howson and Zare (2005) derived exact solutions for the bending response of three-layer beams supported by springs, utilizing a dynamic stiffness matrix approach. Chakrabarti et al. (2011) analyzed laminated beams with soft cores through a finite element method based on higher-order zigzag theory, wherein lateral displacement was modeled quadratically in the core and as constant in the outer layers. Yang et al. (2013) focused on lateral vibrations of axially moving sandwich beams, incorporating shear deformation in the soft-core layer.

Further developments include the work of Bennai et al. (2015), who explored stability analysis of functionally graded beams with thickness variations following a power-law distribution. Sayyad and Ghugal (2017) provided a comprehensive review of bending, vibration, and buckling behavior in multi-layered beams based on several theoretical frameworks, including the layer-wise and zigzag theories. Asgari (2019) employed Reddy's third-order theory to investigate the dynamic instability of sandwich beams on nonlinear foundations under periodic axial loads. Damanpack and Bodaghi (2021) addressed partially delaminated cores in three-layer beams, accounting for nonlinear stiffness behavior at the interface. Additionally, the flexural response of curved laminated structures has been analyzed. Khdeir and Reddy (1997) studied laminated composite shallow arches using shell theory, while Matsunaga (2004) included shear deformation and lateral rotational inertia in analyzing natural frequencies and buckling of circular arches. Lü and Lü (2008) transformed two-dimensional elastic equations to study in-plane vibrations of laminated arches, and Jun et al. (2014) utilized a dynamic stiffness matrix approach to examine shear deformation effects in cross-ply laminated shallow curved beams.

Columns are fundamental structural elements responsible for supporting axial loads. As such, buckling analysis plays a critical role in column design and has long been a focal point of structural research. Several key studies have addressed this phenomenon in diverse contexts. Avcar (2014) examined the elastic buckling of steel columns with square, rectangular, and circular cross-sections under two different boundary conditions. Saracoglu and Uzun (2020) analyzed buckling loads of concrete columns with variable cross-sections, comparing analytical and numerical (ANSYS) results. Lazzari and Batista (2020) investigated the interaction between distortional and global buckling in cold-formed steel lipped channel columns. Qasim and Al-Zaidee (2020) developed a finite element model to simulate post-buckling behavior of cold-formed steel columns using shell elements for structural discretization. Liu et al. (2024) observed that progressive column bending failure often initiates instabilities in geosynthetic-reinforced embankments. Fonseca (2024) focused on square hollow steel columns, both uniform and non-uniform, to derive critical loads and buckling resistance via finite element analysis.

The effect of self-weight is particularly critical in column buckling, as it introduces additional compressive forces that reduce the load-bearing capacity. Columns subjected to significant self-weight are referred to as "heavy columns." Seminal research by Greenhill (1881) addressed the maximum height of a tree under its own weight – arguably the first study conceptualizing the heavy column problem. Wang and Drachman (1981) extended this concept by including both gravitational effects and applied end loads, with particular attention to hanging columns. Virgin et al. (2007) examined a vertically oriented, prismatic cantilever column under linearly varying axial loads induced by self-weight. Lee and Lee (2020) derived and solved the governing equation for buckling length in heavy columns under various boundary conditions. Kanahama et al. (2023) modeled tree self-buckling by incorporating soil-root interaction through rotational springs. Further work by Lee and Lee (2024) analyzed stability in axially non-uniform heavy columns, where mass density and modulus of elasticity varied according to a power-law function. Piyapiphat et al. (2025) examined buckling and post-buckling behavior in cantilever columns composed of axially functionally graded materials influenced by gravity.

Tapered cross-sections are frequently employed in structural systems to optimize material efficiency by tailoring stiffness distribution along the member length. Such configurations reduce material usage while enhancing resistance to instability, especially under variable axial loading. In the context of column buckling, several studies have investigated this effect. Lee and Kuo (1991) developed a simplified method for analyzing elastic stability in rectangular columns with various linear tapering profiles. Fabiani and Mentrasti (2021) addressed buckling of inhomogeneous Euler–Bernoulli

columns with variable cross-sections. Akgöz and Civalek (2022) examined microcolumns made of functionally graded materials with continuously varying cross-sections. Belabed et al. (2024) developed an advanced finite element model based on shear deformation theory for analyzing dynamic behavior in nonuniform sandwich beams.

The shape of a cross-section plays a decisive role in determining a structure's mechanical response under bending, torsion, and axial loading. Among various geometries, elliptical cross-sections are widely used in applications that demand enhanced aerodynamics, directional stiffness, or reduced stress concentration (Ecsedi 2004, Gazal et al. 2017, Sun 2021, Shaka and Padhee 2023).

Flexural rigidity F_r, a key mechanical property for analyzing both static and dynamic behavior, is typically defined as the product of Young's modulus E and the second moment of area I (i.e., $F_r = EI$) (Gere and Timoshenko 1997). However, in LSM cross-sections such as those in bi-material columns, E varies with depth, rendering the classical expression inapplicable. Accordingly, modified formulations for flexural rigidity are necessary and can be approached using concepts similar to those applied in Ludwick-type materials, as discussed by Lee and Lee (2019). Alongside F_r, the mass per unit length D_m becomes an equally important parameter when evaluating buckling performance.

This study addresses the buckling behavior of bi-material composite columns with tapered elliptical cross-sections under self-weight. Emphasis is placed on two aspects: first, the derivation of explicit expressions for flexural rigidity and mass per unit length; second, the application of these expressions in a buckling analysis. A differential equation governing the buckled mode shape is formulated to include both gravitational and taper effects, and numerical methods are used to obtain critical buckling loads and mode shapes.

The novelty of this work lies in the development of explicit stiffness parameters for bi-material composite members and their application to the buckling analysis of heavy tapered columns – an essential aspect of design in various engineering applications.

The following assumptions are made in the formulation:

- Plane sections remain plane after bending.
- No interfacial slippage occurs between constituent materials under bending.
- The column is initially perfect, with no geometric imperfections.
- The axial load is applied at the centroid of the cross-section.
- Thermal effects are neglected.

2 EXPLICIT STIFFNESS OF BI-MATERIAL COMPOSITE CROSS-SECTION

2.1 Neutral axis position

Figure 1(a) illustrates a bi-material composite member possessing an elliptical cross-section, laterally laminated from two hybrid materials and represented within Cartesian coordinates (w, h). The elliptical cross-section features a vertical axis of length d and a horizontal axis of length a. The composite is divided into two distinct regions: the bottom and top sections, with depths h_1 and h_2, respectively, such that the total depth is given by $d = h_1 + h_2$. At the interface $h = h_1$, where the two materials are joined, perfect bonding is assumed, and no slippage occurs under flexural loading.

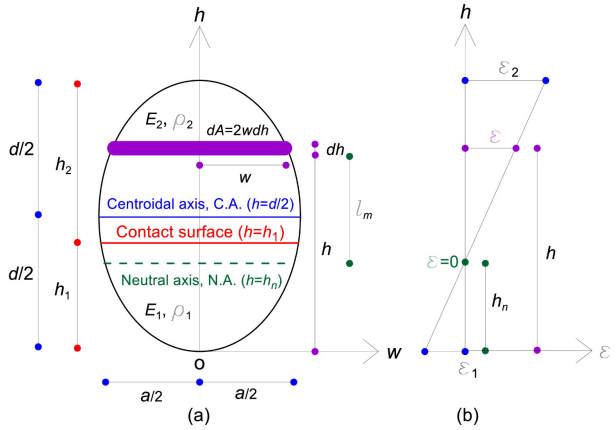

Figure 1 (a) Bi-material composite member with elliptic cross-section and (b) Linear distribution strain ε

The bottom and top materials are characterized by Young's moduli E_1 and E_2, and mass densities ρ_1 and ρ_2, respectively. Due to the asymmetry in material properties and cross-sectional geometry, the centroidal axis (C.A.) and the neutral axis (N.A.) do not coincide.

Figure 1(b) presents the strain distribution ε resulting from bending-induced rotation of the cross-section. Based on the plane section hypothesis, the strain ε varies linearly with respect to the vertical coordinate h throughout the entire depth. At the location of the neutral axis, denoted by $h = h_n$, the strain becomes zero. The strain values at the bottom ($h = 0$) and top ($h = d$) edges are represented by ε_1 and ε_2, respectively.

The modular ratio α and density ratio β are defined as ratios of bi-material properties of the top to bottom composites:

$$\alpha = \frac{E_2}{E_1}, \tag{1}$$

$$\beta = \frac{\rho_2}{\rho_1}. \tag{2}$$

In addition, the bottom depth ratio κ and the neutral position ratio μ are defined as follows:

$$\kappa = \frac{h_1}{d} \leq 1, \tag{3}$$

$$\mu = \frac{h_n}{d} \leq 1. \tag{4}$$

Among the previously introduced ratios, the parameters α, β and κ are predefined, whereas the parameter μ remains unknown and is determined as a function of α, β and κ.

As illustrated in Fig. 1(b), the proportional relationship derived from the two triangles formed by the distribution ε can be expressed as follows:

$$\varepsilon_1 : \varepsilon_2 = h_n : (d - h_n). \tag{5}$$

Utilizing Eqs. (4) and (5), a functional linear equation ε is obtained in terms of the vertical coordinate h:

$$\varepsilon = \varepsilon_1 \left(\frac{h}{\mu d} - 1\right) \text{ for } 0 \leq h \leq d. \tag{6}$$

From the elliptical cross-section geometry in Fig. 1(a), the ellipse equation with the axis lengths of d and a in rectangular coordinates (w, h) is expressed as follows:

$$w = \frac{a}{2}\sqrt{1 - \left(\frac{2h}{d} - 1\right)^2} \text{ for } 0 \leq w \leq a/2 \text{ and } 0 \leq h \leq d. \tag{7}$$

The differential area dA at any vertical position h is given by:

$$dA = 2wdh. \tag{8}$$

The corresponding differential force dF, induced by bending stress over dA, can be expressed as:

$$dF = E\varepsilon dA = 2E\varepsilon wdh, \tag{9}$$

where the Young's modulus E varies depending on the location within the section: $E = E_1$ for regions where $h < h_1$, and $E = E_2$ for regions $h \geq h_1$.

Assuming the neutral axis (N.A.) is located at $h_n = \mu d$, the moment arm length l_m associated with the differential force dF is given by:

$$l_m = |h - \mu d|, \tag{10}$$

where the absolute value reflects the vertical distance from the neutral axis to the location of the force.

The infinitesimal moment dM generated by dF about N.A. is given by:

$$dM = l_m\, dF = 2E\varepsilon w|h - \mu d|dh. \tag{11}$$

To maintain equilibrium, the internal moment produced across the cross-section, obtained by integrating Eq. (11), must be zero. This equilibrium condition is expressed as:

$$\int_0^{h_n} dM + \int_{h_n}^{d} dM = 0. \tag{12}$$

By combining Eqs. (4), (11), and (12), a nonlinear equation is derived in terms of the unknown parameter μ:

$$a\varepsilon_1 \left(E \int_0^{\mu d} f_1 dh + E \int_{\mu d}^{d} f_1 dh\right) = 0. \tag{13}$$

Here, the function f_1 is defined as $f_1 = f_1(h) = (h/\mu d - 1)|h - \mu d|\sqrt{1 - (2h/d - 1)^2}$. Note that the Young's modulus E is piecewise-defined: $E = E_1$ for $h < h_1$, and $E = E_2$ for $h \geq h_1$.

To facilitate use of Eq. (13) in a dimensionless form, a normalized coordinate ζ is introduced:

$$\zeta = \frac{h}{d}. \tag{14}$$

Substituting Eq. (14) into Eq. (13) yields the dimensionless equilibrium equation:

$$\int_0^{\mu} e f_2 d\zeta + \int_{\mu}^{1} e f_2 d\zeta = 0, \tag{15}$$

where the function f_2 is defined as $f_2 = f_2(\zeta) = (\zeta/\mu - 1)|\zeta - \mu|\sqrt{1 - (2\zeta - 1)^2}$ and the parameter e is piecewise-defined: $e = 1$ for $\zeta < \kappa$, and $e = \alpha$ for $\zeta \geq \kappa$.To determine the unknown parameter μ, the bisection method (Burden et al. 2016) was employed, and the trapezoidal rule (Burden et al. 2016) was used to evaluate the integrals numerically.

2.2 Stiffness parameters

In the previous section, the neutral ratio μ was calculated for given input parameters (α, κ). With μ now known, it can be used to evaluate key stiffness properties necessary for structural analysis. Among the various stiffnesses properties, two that are particularly relevant to this study are identified: the flexural rigidity F_r and the mass per unit length D_m, both derived for the bi-material composite cross-section described earlier.

By definition, the flexural rigidity F_r is the product of Young's modulus E and the second moment of area I about N.A. (Gere and Timoshenko 1997). As shown in Fig. 1(a), F_r is calculated by integrating $El_m^2 dA$ across the full cross-section, which includes both the bottom and top materials. The resulting expression is:

$$F_r = E_1 \int_0^{h_1} l_m^2 dA + E_2 \int_{h_1}^{d} l_m^2 dA = aE_1 \left(\int_0^{\kappa d} f_3 dh + \alpha \int_{\kappa d}^{d} f_3 dh\right), \tag{16}$$

where the function f_3 is defined as $f_3 = f_3(h) = (h - \mu d)^2\sqrt{1 - (2h - d)^2}$.

By substituting Eq. (14) into Eq. (16), the expression for the flexural rigidity F_r becomes:

$$F_r = \frac{64}{\pi}\left(\int_0^{\kappa} f_4 d\zeta + \alpha \int_{\kappa}^{1} f_4 d\zeta\right) E_1 I \; = \Gamma_F E_1 I, \tag{17.1}$$

$$\Gamma_F = \frac{64}{\pi}\left(\int_0^{\kappa} f_4 d\zeta + \alpha \int_{\kappa}^{1} f_4 d\zeta\right). \tag{17.2}$$

In this case, the function f_4 is defined as $f_4 = f_4(\zeta) = (\zeta - \mu)^2\sqrt{1-(2\zeta-1)^2}$. The term $I = \pi a d^3/4$ denotes the second moment of area for an elliptical cross-section. The coefficient Γ_F, referred to as the inertia multiplier, is computed via numerical integration using the trapezoidal rule.

Similarly, the mass per unit length D_m of the member shown in Fig. 1(a) is determined analogously to the inertia multiplier:

$$D_m = \rho_1 \int_0^{h_1} dA + \rho_2 \int_{h_1}^{d} dA = \rho_1 \left(\int_0^{\kappa d} dA + \beta \int_{\kappa d}^{d} dA \right) = \Psi_D \rho_1 A, \tag{18.1}$$

$$\Psi_D = \frac{4}{\pi}\left[\int_0^{\kappa} f_5 d\zeta + \beta \int_{\kappa}^{1} f_5 d\zeta \right], \tag{18.2}$$

where the function f_5 is $f_5 = f_5(\zeta) = \sqrt{1-(2\zeta-1)^2}$ and $A = \pi a d$ is the area of the elliptical cross-section. The coefficient Ψ_D, knowns as the mass multiplier, is also obtained using the trapezoidal rule.

2.3 Numerical experiments of explicit stiffness

As a numerical outcome of the stiffnesses analysis conducted in this study, the relationships of (μ, Γ_F, Ψ_D) with respect to input material property ratios (α, β, κ) are presented. These ratios typically depend on the characteristics of the actual structural material used. In numerical experiments, the column parameters are set as $\alpha = 0.6, \beta = 0.5$ and $\kappa = 0.4$ to calculate the stiffness parameters (μ, Γ_F, Ψ_D). The results are illustrated in Figure 2. In each subfigure, one of the three parameters (α, β, κ) varies along the horizontal axis, while the other two remain fixed at the specified values.

In Fig. 2(a), as α increases, both μ and Γ_F increase, exhibiting clearly nonlinear behavior. In contrast, Ψ_D remains constant. In Fig. 2(b), an increase in β leads to a linear increase in Ψ_D, while (μ, Γ_F) remain unaffected. In Fig. 2(c), as κ increases all three parameters (μ, Γ_F, Ψ_D) exhibit nonlinear variations. Notably, at $\kappa = 1$, the values reach $\Gamma_F = 1, \Psi_D = 1$ and $\mu = 0.5$. Interestingly, μ also equals 0.5 at $\kappa = 0$. Additionally, Γ_F demonstrates a non-monotonic trend: it increases initially, then decreases, and increases again as κ varies from 0 to 1.

Numerical experiments are summarized in Table 1 to demonstrate the explicitly formulated stiffness parameters (F_r, D_m) in dimensional units. These calculations are based on two commonly used structural materials: steel and aluminum alloy. The geometric and material properties used in this analysis are as follows: the cross-section and material parameters are:

- ● Cross-sectional geometry (Elliptical cross-section)
  - - $d = 10$ cm for major axis and $a = 6$ cm for minor axis,
  - - $h_1 = 4$ cm for bottom material and $h_2 = 6$ cm for top material,
  - - $A = 4.712 \times 10^{-3}$ m^2 and $I = 2.945 \times 10^{-6}$ m^4.
- ● Material properties
  - - $E_1 = 200$ GPa and $\rho_1 = 7850$ kg/m^3 for bottom material as steel,
  - - $E_2 = 79$ GPa and $\rho_2 = 2800$ kg/m^3 for top material as the aluminum alloy.

Table 1 presents the dimensionless input parameters (α, β, κ), along with their corresponding calculated dimensionless results (μ, Γ_F, Ψ_D), and the explicitly formulated stiffness values (F_r, D_m) in dimensional units. The table also references the specific equations used for computing each stiffness value.

The stiffness parameters (F_r, D_m), derived in this study, can be effectively applied in the structural analysis and design of laterally laminated members composed of two hybrid materials. These explicit values serve as valuable benchmark data for researchers and engineers interested in evaluating or validating related analytical and numerical models.

3 IMPLIMENTATION OF EXPLICIT STIFFNESSES IN BUCKLING ANALYSIS OF HEAVY TAPERED COLUMN

3.1 Governing differential equation

The explicitly derived stiffness parameters (F_r, D_m) from this study are applied to investigate the buckling behavior of columns – an illustrative example showcasing the use of explicit stiffness in bending analysis. However, the

implementation of these parameters is not limited to buckling problems; it also provides a foundation for analyzing a wide range of structural behaviors, including both static and dynamic bending scenarios.

As illustrated in Fig. 3(a), the initial, unbuckled state of a straight column of length l is shown as a dashed line. The column is assumed to be perfect, meaning it is free of initial imperfections, and it features a bi-material composite cross-section as defined in the previous section. The column can be supported under various end conditions, including hinged, clamped, and free supports. As a result, four end constraint configurations are considered: hinged-hinged, hinged-clamped, clamped-clamped and free-clamped. In each case, the first term denotes the top-end support, and the second term denotes the bottom-end support.

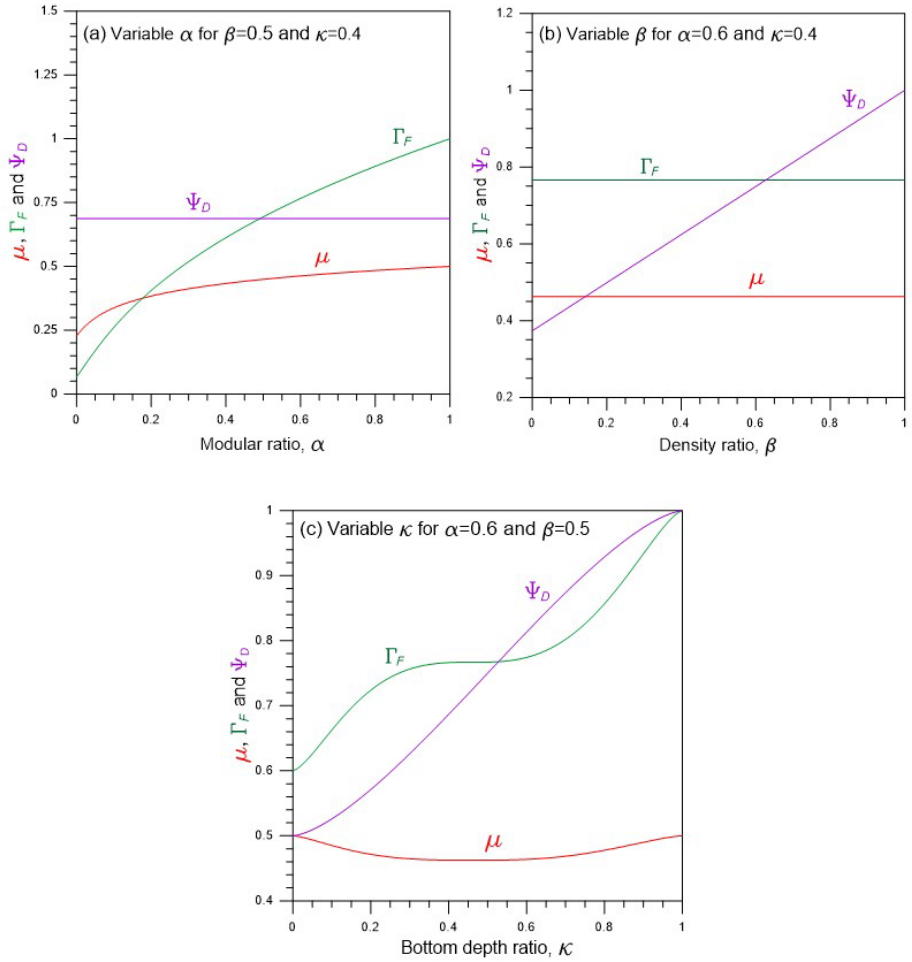

Figure 2 (μ, Γ_F, Ψ_D) versus (α, β, κ) curves for: (a) variable α, (b) variable β and (c) variable κ

Table 1 Numerical experiments of explicit properties of bi-material composite member.

Explicit property	Relevant equation	Value
Modular ratio α	Equation (1)	0.3950
Density ratio β	Equation (2)	0.3567
Bottom depth ratio κ	Equation (3)	0.4
Neutral position ratio μ	Equation (4)	0.4321
Inertia multiplier Γ_F	Equation (17.2)	0.6080
Mass multiplier Ψ_D	Equation (18.2)	0.5970
Neutral axis position h_n	Equation (4)	4.321 cm
Flexural rigidity F_r	Equation (17.1)	358.11 kN·m^2
Mass per unit length D_m	Equation (18.1)	22.083 kg/m

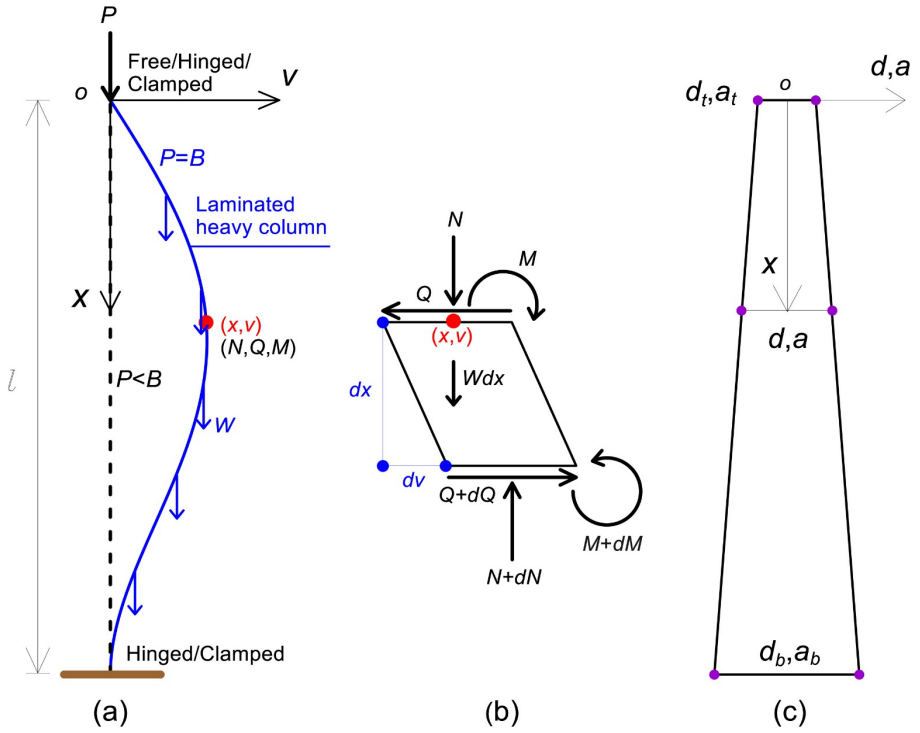

Figure 3 (a) Geometry of buckled heavy column, (b) Free body diagram of buckled column element and (c) Linearly varying taper function along column axis

The column has a tapered elliptical cross-section, with both major and minor axis lengths varying along the vertical coordinate x in Fig. 3(a). The corresponding stiffness properties (F_r, D_m), which are functions of the cross-sectional geometry and material composition, have already been determined in the earlier section.

An axial load P is applied at the midpoint of the neutral axis, producing compressive stress along the column's length. It is assumed that no slippage occurs along the material interface due to bending. In addition to the applied load P, the self-weight of the column W is also considered. This introduces a gravitational prestress, increasing the overall axial compressive force. In structural mechanics, a column whose self-weight is considered in the buckling analysis is referred to as a heavy column.

When the applied load P is less than the critical buckling load B, the column remains stable and unbuckled – its axis remains straight, as depicted by the dashed line in Fig. 3(a). However, as P increases and reaches the critical value B (i.e., $P = B$), the column loses stability and undergoes buckling. This results in an elastic deflection of the column, described by the buckled mode shape in Cartesian coordinates (x, v), where v represents the lateral displacement. Once buckled under the combined effects of external load P and self-weight W, the column develops internal stress resultants, including an axial force N, a shear force Q and a bending moment M which act across the cross-section and govern the column's post-buckling response.

Figure 3(b) illustrates the free-body diagram of a differential element of the buckled column. The diagram shows the stress resultants of axial force N, shear force Q, and bending moment M as well as the distributed self-weight W, which acts along the axial direction. From this free-body diagram, the axial force equilibrium: $\sum F_x = (N + dN) - N - Wdx = 0$, the shear force equilibrium: $\sum F_v = (Q + dQ) - Q = 0$ and the moment equilibrium: $\sum M = (M + dM) - M + Qdx + Ndv = 0$ can be set and the revised versions of these three equilibriums are:

$$\frac{dN}{dx} - W = 0, \tag{19}$$

$$\frac{dQ}{dx} = 0, \tag{20}$$

$$\frac{dM}{dx} + N\frac{dv}{dx} + Q = 0. \tag{21}$$

Here, in above equations, W denotes the axially varying self-weight (i.e., force per unit axial length), and the compressive axial force N is considered positive.

Differentiating Eq. (21) with respect to x yields a second-order derivative of the bending moment:

$$\frac{d^2M}{dx^2} = -N\frac{d^2v}{dx^2} - \frac{dN}{dx}\frac{dv}{dx} - \frac{dQ}{dx}. \tag{22}$$

Substituting Eqs. (19) and (20) into Eq. (22), the expression simplifies to:

$$\frac{d^2M}{dx^2} = -N\frac{d^2v}{dx^2} - W\frac{dv}{dx}. \tag{23}$$

Next, considering both the self-weight W and axial force N in Eq. (23), the self-weight W can be derived from the mass per unit length D_m as defined in Eq. (18.1), by incorporating gravitational acceleration g:

$$W = D_m g = \Psi_D \rho_1 g A. \tag{24}$$

Substituting Eq. (24), the axial force N can be expressed as:

$$N = B + \int_0^x W dx = B + \Psi_D \rho_1 g A x. \tag{25}$$

By substituting Eqs. (24) and (25) into Eq. (23), the resulting expression is:

$$\frac{d^2M}{dx^2} = -(B + \Psi_D \rho_1 g A x)\frac{d^2v}{dx^2} - \Psi_D \rho_1 g A \frac{dv}{dx}. \tag{26}$$

The bending moment M is related to the transverse deflection v and the flexural rigidity F_r, which can be rewritten using Eq. (17.1) as (Gere and Timoshenko 1997):

$$M = F_r \frac{d^2v}{dx^2} = \Gamma_F E_1 I \frac{d^2v}{dx^2}, \tag{27}$$

where F_r is expressed as $\Gamma_F E_1 I$.

From Eq. (27), the following second derivative d^2M/dx^2 is obtained:

$$\frac{d^2M}{dx^2} = \Gamma_F E_1 \left(\frac{d^2I}{dx^2}\frac{d^2v}{dx^2} + 2\frac{dI}{dx}\frac{d^3v}{dx^3} + I\frac{d^4v}{dx^4}\right). \tag{28}$$

Finally, substituting Eq. (28) into Eq. (26) yields the governing fourth-order ordinary differential equation:

$$\Gamma_F E_1 I \frac{d^4v}{dx^4} = -\Gamma_F E_1 \left(\frac{d^2I}{dx^2}\frac{d^2v}{dx^2} + 2\frac{dI}{dx}\frac{d^3v}{dx^3}\right) - (B + \Psi_D \rho_1 g A x)\frac{d^2v}{dx^2} - \Psi_D \rho_1 g A \frac{dv}{dx}. \tag{29}$$

This study focuses on tapered columns, in which both the cross-sectional area A and the second moment of area I in Eq. (29) vary along the axial coordinate x. Figure 3(c) illustrates the changes in the major and minor axes, denoted as d and a, respectively, of the elliptical cross-section, represented in rectangular coordinates (x, d) or (x, a).

The major and minor axis lengths at the top of the column $(x = 0)$ are represented by d_t and a_t, while those at the bottom $(x = l)$ are denoted as d_b and a_b. To characterize the variation in geometry along the column, a taper ratio λ is introduced, defined as the ratio of the top axis length to the bottom axis length:

$$\lambda = \frac{d_t}{d_b} = \frac{a_t}{a_b} \leq 1. \tag{30}$$

In this analysis, the taper ratio is assumed to satisfy $\lambda \leq 1$, indicating that the material or structural capacity at the bottom is greater than or equal to that at the top. If $\lambda > 1$, the configuration of the top and bottom sections should be reversed to maintain the intended structural assumptions.

The taper configuration defined by Eq. (30) allows for a wide range of geometric variations, including linear, quadratic, exponential, and trigonometric profiles. In the present study, a linear taper is adopted, as illustrated in Fig. 3(c). Based on Eq. (30), the linear variation of the major and minor axes d and a along the axial coordinate x is expressed as:

$$d = d_b\left[(1-\lambda)\frac{x}{l}+\lambda\right] = d_b f_6, \tag{31.1}$$

$$a = a_b\left[(1-\lambda)\frac{x}{l}+\lambda\right] = a_b f_6, \tag{31.2}$$

where the taper function is defined as $f_6 = f_6(x) = [(1-\lambda)\,x/l+\lambda]$.

Using Eqs. (31.1) and (31.2), the cross-sectional area A and second moment of area $I$of the elliptical section at a given position x can be expressed as:

$$A = \frac{\pi}{4}ad = \frac{\pi}{4}a_b d_b f_6^2 = A_b f_6^2, \tag{32}$$

$$I = \frac{\pi}{64}ad^3 = \frac{\pi}{64}a_b d_b^3 f_6^4 = I_b f_6^4. \tag{33}$$

In these expressions, A_b and I_b represent the area and the second moment of area at the bottom end of the column $(x = l)$, respectively, with $A_b = (\pi/4)a_b d_b$ and $I_b = (\pi/64)a_b d_b^3$.

Using Eq. (33), the following expressions for the first and second derivatives of the second moment of area I with respect to x are derived:

$$\frac{dI}{dx} = I_b\frac{df_6^4}{dx} = 4(1-\lambda)\frac{I_b}{l}f_6^3 = 4e_1\frac{I_b}{l}f_6^3, \tag{34.1}$$

$$\frac{d^2I}{dx^2} = 4e_1\frac{I_b}{l}\frac{d^2f_6^3}{dx^2} = 12e_1^2\frac{I_b}{l^2}f_6^2, \tag{34.2}$$

where $e_1 = 1-\lambda$.

By substituting Eqs. (32), (33), (34.1), and (34.2) into Eq. (29), the following fourth-order ordinary differential equation is obtained. This equation governs the buckling mode shape of a heavy, linearly tapered column composed of two hybrid materials:

$$\Gamma_F E_1 I_b f_6^4\frac{d^4v}{dx^4} = -\Gamma_F E_1 I_b\left(\frac{12e_1^2}{l^2}f_6^2\frac{d^2v}{dx^2}+\frac{8e_1}{l}f_6^3\frac{d^3v}{dx^3}\right) - (B+\Psi_D\rho_1 g A_b x f_6^2)\frac{d^2v}{dx^2} - \Psi_D\rho_1 g A_b f_6^2\frac{dv}{dx}. \tag{35}$$

To generalize the theoretical formulation based on the numerical results obtained in this study, the following nondimensional variables are introduced:

$$\xi = \frac{x}{l}, \tag{36}$$

$$\eta = \frac{v}{l}, \tag{37}$$

$$\gamma = \frac{\rho_1 g A_b l^3}{E_1 I_b}, \tag{38}$$

$$b = \frac{Bl^2}{E_1 I_b}. \tag{39}$$

In this context, (ξ,η) represent the normalized spatial and deflection coordinates, respectively. The γ denotes the self-weight parameter while b corresponds to the buckling load parameter.

By applying the nondimensional parameters defined earlier, the dimensional form of Eq. (35) is transformed into the following dimensionless fourth-order differential equation:

$$\frac{d^4\eta}{d\xi^4} = -\frac{8e_1}{f_7}\frac{d^3\eta}{d\xi^3} - \left(\frac{b}{\Gamma_F}\frac{1}{f_7^4} + \frac{12e_1^2}{f_7^2} + \gamma\frac{\Psi_D}{\Gamma_F}\frac{\xi}{f_7^2}\right)\frac{d^2\eta}{d\xi^2} - \gamma\frac{\Psi_D}{\Gamma_F}\frac{1}{f_7^2}\frac{d\eta}{d\xi} \text{ for } 0 \le \xi \le 1. \quad (40)$$

Here, $f_7 = f_7(\xi) = e_1\xi + \lambda$. In this formulation b represents the eigenvalue associated with the buckling load and must be determined by solving the differential equation.

The boundary conditions corresponding to the dimensionless differential equation are described below. At a hinged end ($x = 0$ or $x = l$), both transverse deflection v and the bending moment $M(= F_R\, d^2v/dx^2)$ are zero. The associated nondimensional boundary conditions are given as:

$$\text{Hinged end } (\xi = 0 \text{ or } \xi = 1): \eta = 0, \frac{d^2\eta}{d\xi^2} = 0. \quad (41)$$

At a clamped end ($x = 0$ or $x = l$), both the deflection v and its slope dv/dx vanish. This leads to the following nondimensional boundary conditions:

$$\text{Clamped end } (\xi = 0 \text{ or } \xi = 1): \eta = 0, \frac{d\eta}{d\xi} = 0. \quad (42)$$

At a free end ($x = 0$), where both the bending moment M and shear force Q (as defined in Eq. (21)) are zero, the corresponding nondimensional boundary conditions are:

$$\text{Free end } (\xi = 0): \frac{d^2\eta}{d\xi^2} = 0, \frac{d^3\eta}{d\xi^3} + \frac{b}{\lambda^4\Gamma_F}\frac{d\eta}{d\xi} = 0. \quad (43)$$

It is important to note that this study does not consider configurations with a free end located at the bottom ($\xi = 1$), such as hanging columns.

3.2 Numerical methods for solving governing equation

The parameters relevant to the buckling analysis include the end constraint conditions, span length l, the major and minor axis lengths at the top and bottom (d_t, a_t) and (d_b, a_b), section depths (h_1, h_2), Young's moduli (E_1, E_2), and mass densities (ρ_1, ρ_2). These input values are utilized to derive the dimensionless parameters previously introduced: the modular ratio α, density ratio β, bottom depth ratio κ, self-weight parameter γ and taper ratio λ.

Due to the absence of a closed-form solution for the dimensionless differential Eq. (40), numerical techniques must be employed to compute the buckling load parameter b, which serves as an eigenvalue associated with the buckled mode shape (ξ, η). The Runge-Kutta method (Burden et al. 2016) is adopted to numerically integrate Eq. (40) for determining the displacement field (ξ, η), while the Regula-Falsi method (Burden et al. 2016) is utilized to identify the corresponding eigenvalue b. These numerical methods have been successfully applied in existing literature (Kim et al. 2023). The computational algorithm developed in this study follows a systematic procedure to determine the eigenvalue b and the associated mode shape (ξ, η) as outlined in the subsequent steps.

1. Specify the column parameters $(\alpha, \beta, \kappa, \gamma, \lambda)$ along with the end constraints.
2. Calculate the stiffness-related parameters (Γ_F, Ψ_D) using the given values of (α, β, κ).
3. Assign an initial trial value for the buckling load parameter b, starting with $b = 0$.
4. Numerically integrate the dimensionless differential Eq. (40) over the range $0 \le \xi \le 1$ using the Runge-Kutta method. Apply the initial conditions at $\xi = 0$ as specified in the boundary conditions (Eds. (41)–(43)) to compute the trial mode shape (ξ, η).
5. Evaluate the determinant D by applying the boundary conditions at $\xi = 1$. The convergence criterion is defined as:

$$|D| \le 1 \times 10^{-7}. \quad (44)$$

If this condition is satisfied, terminate the computation and record the eigenvalue b along with the corresponding mode shape (ξ, η).

6. If the criterion is not met, increment the trial value of b by a specified amount Δb, and return to Step 2 with the updated trial value $b(\leftarrow b + \Delta b)$.

7. During the iteration process in Steps 2 to 5, monitor the sign of the product $D_1 \times D_2$, where D_1 and D_2 are the determinant values from the previous and current iterations, respectively.

8. If the sign of $D_1 \times D_2$ is negative, a root lies in the interval $b_1 \leq b \leq b_2$, where b_1 and b_2 are the trial values corresponding to D_1 and D_2. The next trial value b_3 is computed using the Regula-Falsi method:

$$b_3 = \frac{b_1|D_2| + b_2|D_1|}{|D_1| + |D_2|}. \tag{45}$$

9. Repeat Step 7 until the following condition is satisfied:

$$\frac{b_2 - b_1}{b_2} \leq 1 \times 10^{-5}. \tag{46}$$

10. Once the convergence condition in Step 9 is met, terminate the computation and output the converged eigenvalue b together with the associated buckled mode shape (ξ, η).

A FORTRAN program was developed to implement the numerical methods used for calculating the buckling load parameter b, along with the associated variables (ξ, η). This program includes subroutines to compute the stiffness matrices (Γ_F, Ψ_D), as defined in the previous section. Since b is approximated as an eigenvalue using the numerical methods mentioned earlier, it is crucial to adjust the step size $\Delta\xi$ in the Runge–Kutta method to ensure accurate integration of Eq. (40) before conducting numerical experiments.

A convergence analysis was carried out by varying $\Delta\xi$ to evaluate the accuracy of the computed b. Figure 4 presents the results for four different boundary conditions and includes the relevant column parameters. The results demonstrate that the computed values of b converge effectively when $1/\Delta\xi = 10$. For example, in the case of the hinged–clamped condition, the trial eigenvalue $b = 7.5727$ obtained with $1/\Delta\xi = 10$ closely approaches the target value $b = 7.5688$ achieved at $1/\Delta\xi = 200$, corresponding to a convergence ratio of 0.9995 (i.e., $7.5688/7.5727$).

For the numerical calculations in this study, a value of $1/\Delta\xi = 20$ was used, yielding results with an accuracy of five significant digits for the target value $b = 7.5688$, comparable to the accuracy achieved with $1/\Delta\xi = 200$. The FORTRAN code developed in this work efficiently computes the buckling load parameter b in an average time of less than 0.011 seconds per solution on a standard PC (LG LAM8G/SSD256G/WIN10).

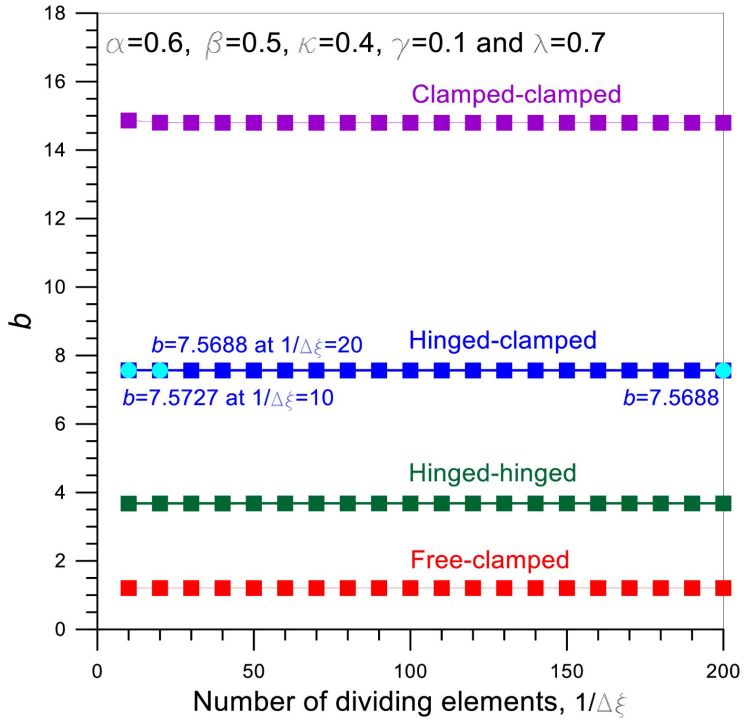

Figure 4 Convergence analysis for Runge-Kutta method

3.3 Numerical experiments and discussion

The first numerical study compares the bucking loads b from this study and open literature for validation purposes. Comparisons b are reported in Table 2 for homogeneous columns with circular cross-section ($d = a$) and Table 2 for the nonhomogeneous tapered columns considered in this study. In the first case, the verification considers homogeneous columns ($\kappa = 1$) without self-weight ($\gamma = 0$) for three end constraints. The buckling load parameters b from this study and Riley's results are compared in Table 2, revealing a strong correspondence. These comparisons validate the theory presented, excluding the explicit stiffness of the laminated members formulated in previous section. For convenience, the equation of b as a function of the taper ratio λ by Riley (2003) is presented in this table.

Table 2 Comparison of buckling load parameter b between this study and reference for homogeneous column with circular cross-section ($d = a$) without self-weight ($\kappa = 1$ and $\gamma = 0$).

End constraint	Taper ratio λ	Buckling load parameter b		Eqs. of buckling load parameter b by Riley (2003)
		This study	Riley (2003)	
Hinged–hinged	0.5	2.4674	2.4672	$b = 0.9997\lambda^{1.9997}\pi^2$
Hinged–clamped	0.4	3.2305	3.2305	$b = 0.9990\lambda^{1.9994}(\pi/0.699)^2$
Free–clamped	0.3	0.4929	0.4928	$b = 1.2110\lambda^{1.4969}(\pi/2)^2$

In the second case, the verification focuses on heavy, tapered laminated columns. The material properties – steel for the bottom layer and aluminum alloy for the top layer – are specified in Table 1. The column has a span length of $l = 2$ m. The elliptical cross-section varies linearly along the length, with the major axis lengths set as $d_b = 10$cm and $d_t = 7$cm, and the minor axis lengths as $a_b = 6$ cm and $a_t = 4.2$ cm, in accordance with the linear variation defined by Eqs. (31.1) and (31.2). The values $d = 10$ cm and $a = 6$ cma used in Table 1 correspond to d_b and a_b, which are applied in the calculation of the buckling load.

Although the two material layer depths, h_1 and h_2, vary along the column due to the changing d, the dimensionless parameters ($\alpha, \beta, \kappa, \mu, \Gamma_F, \Psi_D$) remain constant, as shown in Table 1. The remaining parameters are calculated as $\lambda = 0.7$ using Eq. (30) and $\gamma = 4.924 \times 10^{-3}$ using Eq. (38). The actual buckling load B can be obtained from the dimensionless value b computed in this study using Eq. (39) as $B = 147.26b$ kN.

The ADINA (2017) was used to obtain finite element method (FEM) solutions, modeling the column as a two-dimensional axial member appropriate for the planar structure under consideration. The effect of self-weight was modeled as a downward nonuniform load distribution.

The buckling loads B were calculated for all four end constraint conditions using both the proposed method and FEM, with the results compared in Table 3. The two sets of results show excellent agreement, with discrepancies within a 2% error margin. The percentage error is defined as Error (%) = (1−FEM/This study) × 100.

Table 3 Comparison of buckling load B from this study and ADINA for heavy tapered column.

End constraint	Buckling load B in kN		Error (%)
	This study	ADINA (2017)	
Hinged–hinged	432.89	426.61	1.45
Hinged–clamped	885.79	874.01	1.33
Clamped–clamped	1732.0	1710.4	1.25
Free–clamped	142.74	140.38	1.65

These comparisons validate the theoretical and numerical methods developed in this study, which account for member stiffness, tapering, and self-weight effects. It is noted that the buckling loads B predicted by this study consistently overestimate those obtained from the ADINA FEM solutions.

Tables 2 and 3 analyze the influence of end constraints on the buckling load parameter b. Specifically, Table 2 presents the result for homogeneous columns, while Table 3 focuses on laminated columns, detailing the minimum and maximum buckling loads under free-clamped and clamped-clamped boundary conditions, respectively. As indicated in Table 3, a substantial variation in buckling load arises due to the type of end restraint. In particular, the clamped-clamped configuration yields a buckling load approximately 12.13 times greater than that of the free-clamped case, underscoring

the critical role of boundary condition stiffness. Moreover, the buckling load for the clamped-clamped condition surpasses that of the hinged-clamped case, despite both configurations sharing a clamped lower end.

In subsequent numerical simulations, unless otherwise specified in tables and figures, the following parameter values are adopted consistently: $\alpha = 0.6$, $\beta = 0.5$, $\kappa = 0.4$, $\gamma = 0.1$ and $\lambda = 0.7$. Figure 5 depicts the relationship between the buckling load b and the modular ratio α. An upward trend in b is observed as α increases, irrespective of the end boundary conditions. When $\alpha = 0.6$, the column effectively behaves as a homogeneous material characterized by $E_t = 0$, whereas $\alpha = 1$ corresponds to the case where the material properties align with $E_t = E_b$. This progression in material orientation leads to a monotonic increase in b with increasing α.

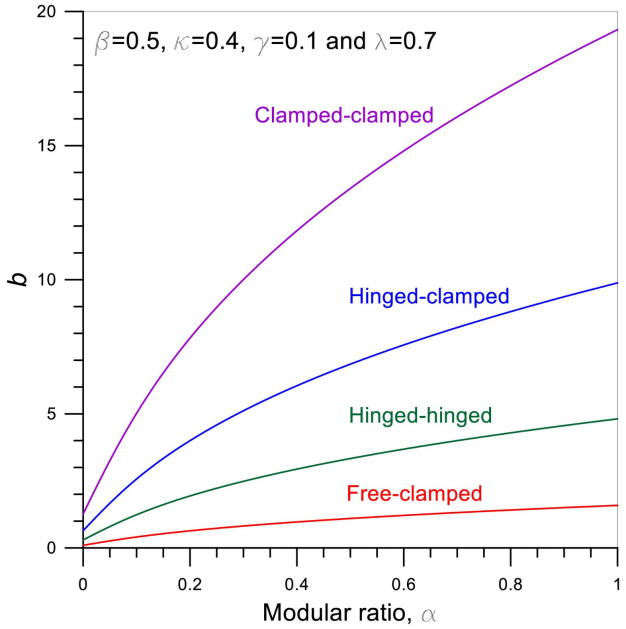

Figure 5 b versus α curve

Figure 6 illustrates the variation in buckling load b as a function of the density ratio β. As expected, b decreases with increasing β, regardless of the end constraints, because the increased mass associated with higher β value reduces the column's buckling resistance. Overall, the influence of β on b is relatively limited. For instance, for the clamped-clamped ends, the reduction rate from $\beta = 0$ to $\beta = 1$ (the maximum value of β) is only 0.0128 ($= 1 - 14.794/14.813$), which is very small (see the two points marked by ●), indicating that the effect of β is negligible.

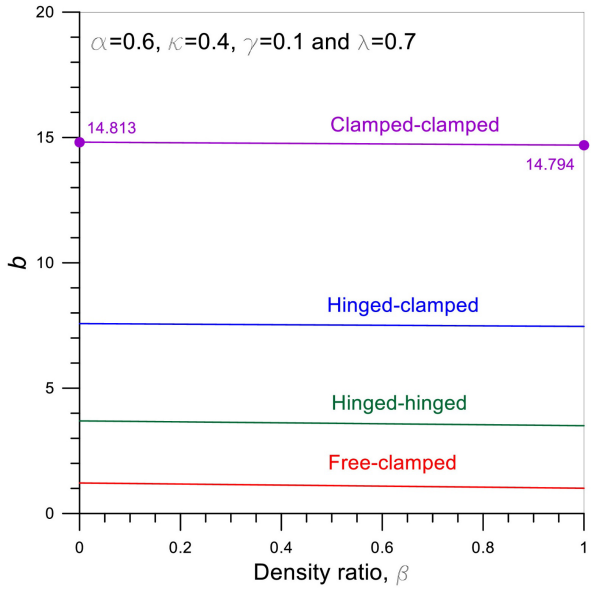

Figure 6 b versus β curve

Figure 7 presents the buckling load b as a function of the bottom depth ratio κ. Generally, as κ increases, b also increases. However, there is a short range where b decreases very slightly. For example, for a clamped-clamped end constraint, $b$decreases with increasing κ in the range $0.451 < \kappa < 0.457$, corresponding to $14.814 > b > 14.812$. This decreasing effect is negligible. This non-monotonic behavior is attributed to the influence of the stiffness components Γ_F and Ψ_D, as shown in Fig. 2(c), which exhibit a similar pattern of variation with respect to κ. These stiffness trends directly affect the buckling response and correspond to the patterns illustrated in Fig. 2.

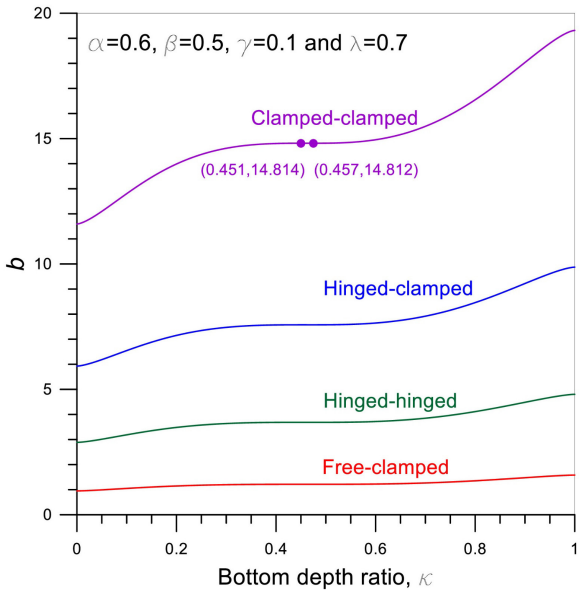

Figure 7 b versus κ curve

Figure 8 illustrates the buckling load b as a function of the self-weight parameter γ. As γ increases, a gradual decrease in b is observed. This trend is primarily due to the corresponding rise in axial force N resulting from increased self-weight. Overall, the influence of γ on b remains relatively modest.

Figure 9 illustrates the relationship between the buckling load b and the taper ratio λ. As λ increases, b also increases. This behavior is consistent with the expectation that greater structural tapering enhances column strength, thereby improving buckling resistance. Notably, when $\lambda = 0$, the column is unable to support external loading, as indicated by $b = 0$, signifying a complete loss of load-bearing capacity in the untapered configuration.

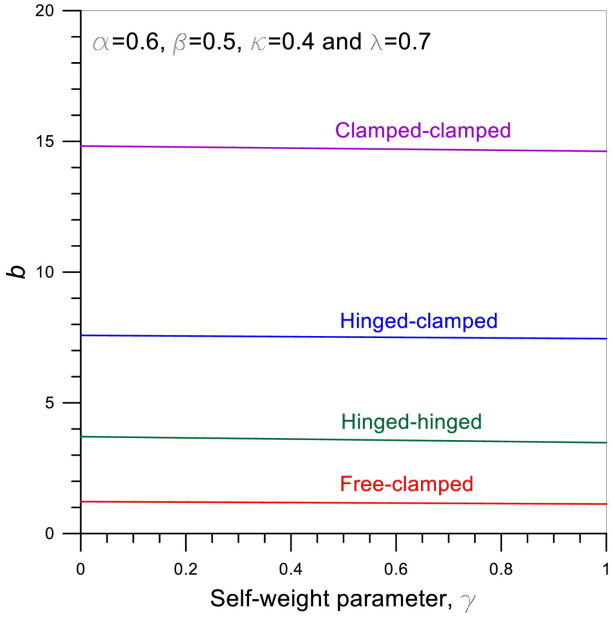

Figure 8 b versus γ curve

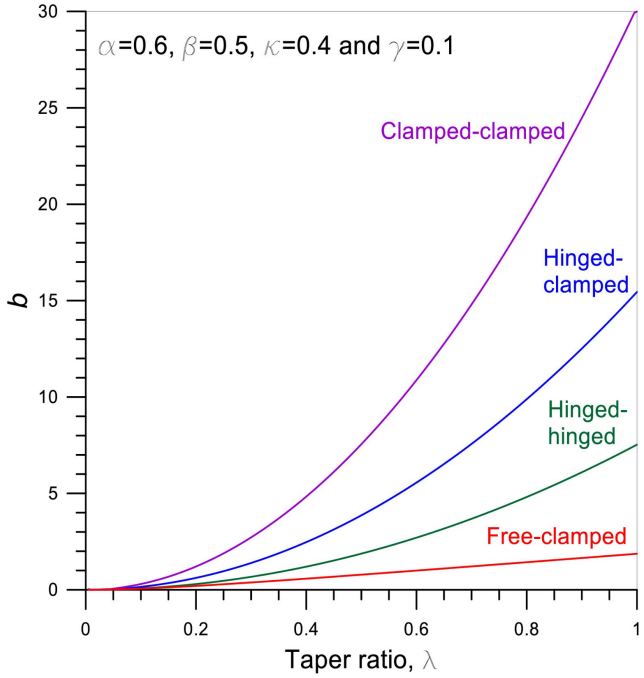

Figure 9 b versus λ curve

Figure 10 illustrates the buckling mode shapes (ξ, η), each associated with corresponding values of b, under the given column parameters. The boundary conditions specified in Eqs. (41) - (43) are effectively reflected in the mode shapes at both the top end $(\xi = 0)$ and the bottom end $(\xi = 1)$, as shown in the figure. These mode shapes are particularly valuable for structural analysis and design, as they reveal critical information such as the relative amplitudes, nodal positions, and locations of maximum deflection along the column.

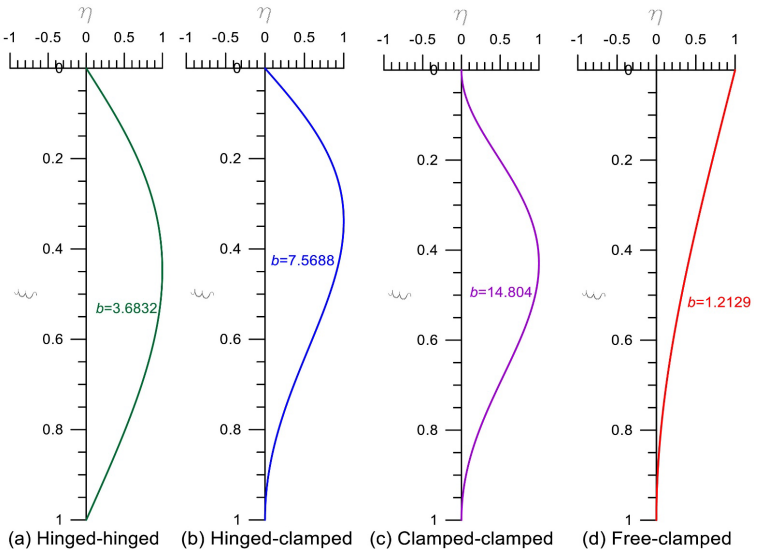

Figure 10 Example of buckling mode shapes by end constraint with $\alpha = 0.6, \beta = 0.5, \kappa = 0.4, \gamma = 0.1$ and $\lambda = 0.7$

4 Conclusions

This study has examined the application of explicit stiffness formulations to laterally laminated members composed of two hybrid materials, specifically in the context of column buckling analysis. The research focused on two primary aspects: (1) the derivation of explicit stiffness parameters for columns with elliptical cross-sections – particularly flexural rigidity and mass per unit length – and (2) the integration of these stiffness characteristics into the flexural buckling analysis under axial compressive forces.

The governing differential equation for buckling includes both the self-weight of the column – thus treating it as a "heavy column" – and a linear tapering effect along its length. A numerical solution methodology was developed to solve this equation and obtain the corresponding buckling loads and mode shapes.

Comprehensive parametric studies were conducted to investigate the influence of various factors, such as boundary conditions, modular ratio, density ratio, bottom depth ratio, self-weight parameter, and taper ratio. These results are presented through detailed tables and graphical representations. Key findings from the numerical analysis include:

- When applying the Runge-Kutta method with the column length discretized into 20 segments, the buckling load results converged, yielding five-digit accuracy.
- The computed buckling loads show strong agreement with established results from Riley (2003) and ADINA (2017).
- Buckling loads increase with higher modular ratios.
- Buckling loads decrease as the density ratio increases.
- A non-monotonic behavior is observed with changes in the bottom depth ratio: buckling loads initially rise, then fall, and rise again.
- Increased self-weight parameters result in reduced buckling loads.
- Buckling resistance improves with an increase in the taper ratio.

Looking forward, future research should extend the use of explicit stiffness formulations beyond the scope of buckling analysis. Potential applications include stress and strain analysis, stability evaluation, nonlinear behavior assessment, and optimization in both static and dynamic structural analyses.

Acknowledgements

This work is supported by the National Research Foundation of Korea (NRF) (Grant No. NRF-RS-2025-24523111).

Author's Contributions: Conceptualization, BK Lee; Methodology, JK Lee, SJ Oh; Investigation, SJ Oh; Writing - original draft, BK Lee; Writing - review & editing, JK Lee; Funding acquisition, JK Lee; Resources, BK Lee, SJ Oh.

Data Availability: Research data is only available upon request.

Editor: Pablo Andrés Muñoz Rojas

References

ADINA (2017). *ADINA 9.3.* Watertown, MA, USA: ADINA R & D, Inc.

Akgöz, B. & Civalek, Ö. (2022). Buckling analysis of functionally graded tapered microbeams via Rayleigh-Ritz method. *Mathematics*, 10:4429.

Asgari, S. (2019). Dynamic instability and free vibration behavior of three-layered soft-cored sandwich beams on elastic foundations. *Struct Eng Mech*, 72:525–540.

Avcar, M. (2014). Elastic buckling of steel columns under axial compression. *Am J Civil Eng*, 2(3):102–108.

Belabed, Z., Tounsi, A. & Bousahla, A. (2024). Accurate free and forced vibration behavior prediction of functionally graded sandwich beams with variable cross-section: A finite element assessment. *Mech Based Des Struct Mach*, 52:9144–9177.

Bennai, R., Atmane, H. A. & Tonis, A. (2015). New higher-order shear and normal deformation theory for functionally graded sandwich beam. *Steel Compos Struct*, 19:521–546.

Burden, R. L., Faires, D. J. & Burden, A. M. (2016). *Numerical analysis.* Boston, MA, USA: Cengage Learning.

Chakrabarti, A., Chalak, H. D., Iqbal, M. A. & Sheikh, A. H. (2011). A new FE model based on higher order zigzag theory for the analysis of laminated sandwich beam with soft core. *Compos Struct*, 93:271–279.

Damanpack, A. R. & Bodaghi, M. (2021). A new sandwich element for modelling partially delaminated sandwich beam structures. *Compos Struct*, 256:113068.

Ecsedi, I. (2004). Elliptic cross section without warping under torsion. *Mech Res Commun*, 31(2):147–150.

Fabiani, M. & Mentrasti, L. (2021). Exact solutions of linear buckling for a class of FGM columns with varying cross-section. *Int J Struct Stab Dyn*, 21:2150079.

Fonseca, E. M. M. (2024). Stability analysis of steel columns with fixed-free ends under axial compression: Uniform and non-uniform square hollow sections. *J Civil Hydra Eng*, 2(2):109–119.

Gazal, M., Groper, M. & Gendelman, O. (2017). Analytical, experimental and finite element analysis of elliptical cross-section helical spring with small helix angle under static load. *Int J Mech Sci*, 130:476–486.

Gere, J. M. & Timoshenko, S. P. (1997). *Mechanics of materials.* Boston, MA, USA: PWS Publishing Company.

Greenhill, A. G. (1881). Determination of the greatest height consistent with stability that a vertical pole or mast can be made, and the greatest height to which a tree of given proportions can grow. *Math Proc Camb Philos Soc*, 1:65–73.

Howson, W. P. & Zare, A. (2005). Exact dynamic stiffness matrix for flexural vibration of three-layered sandwich beam. *J Sound Vib*, 282:753–767.

Jun, L., Guangwei, R., Jin, P., Xiaobin, L. & Weiguo, W. (2014). Free vibration analysis of a laminated shallow curved beam on trigonometric shear deformation theory. *Mech Based Des Struct Mach*, 42(1):111–129.

Kanahama, T., Chalermsin, C. L. & Sato, M. (2023). Mechanical instability of heavy column with rotational spring. *J Mech*, 39(3):480–490.

Khdeir, A. & Reddy, J. N. (1997). Free and forced vibration of cross-ply laminated composite shallow arches. *Int J Solids Struct*, 34(10):1217–1234.

Kim, G. S., Lee, J. K., Ahn, D. S. & Lee, B. K. (2023). Free vibration and buckling of laterally functionally graded material column. *Mech Compos Mater*, 59(4):1–18.

Lazzari, J. A. D. & Batista, E. M. (2020). Buckling analysis, structural behavior and strength of distortional-global interaction in cold-formed steel lipped channel columns. Proc Cold-Formed Steel Res Consort Colloquium, 33.

Lee, B. K. & Lee, J. K. (2019). Generalized second moment of areas of regular polygons for Ludwick type material and its application to cantilever column buckling. *Int J Struct Stab Dyn*, 19(2):1950010.

Lee, B. K. & Lee, J. K. (2024). Stability analysis of axially functionally graded heavy column. *J Compos Mater*, 60:335–352.

Lee, J. K. & Lee, B. K. (2020). Buckling lengths of heavy columns with various end conditions. *Eng Solid Mech*, 8(2):163–168.

Lee, S. Y. & Kuo, Y. H. (1991). Elastic stability of non-uniform columns. *J Sound Vib*, 148(1):11–24.

Liu, H., Luo, Q., El-Naggar, M. H., Liu, K. & Wang, T. (2024). Evaluating stability of rigid column-supported and geosynthetic-reinforced embankments. *Geosynth Int*, 31(5):711–727.

Lü, Q. & Lü, C. (2008). Exact two-dimensional solutions for in-plane natural frequencies of laminated circular arches. *J Sound Vib*, 318(4):982–990.

Matsunaga, H. (2004). Free vibration and stability of laminated composite circular arches subjected to initial axial stress. *J Sound Vib*, 271(3):651–670.

Piyapiphat, S., Nuntasri, A., Phungpaingam, B., Musiket, K., Jiammeepreecha, W. & Chucheepsakul, S. (2025). Inference of self-weight on buckling and post-buckling behavior of AFGM spring-hinged cantilever column under tip load. *Mech Based Des Struct Mach*, 53(7):5316–5340.

Qasim, T. M. & Al-Zaidee, S. R. (2020). Post-buckling analysis of cold-form steel column. *J Eng*, 26(4):173–187.

Riley, C. E. (2003). Elastic buckling loads of slender columns with variable cross-section by Newark Method. *MS Thesis*. Fort Collins, Colorado, USA: Colorado State University.

Saracoglu, M. H. & Uzun, S. (2020). Stability analysis of columns with variable cross-sections. *J Struct Eng Appl Mech*, 3(3):169–179.

Sayyad, A. S. & Ghugal, Y. M. (2017). Bending, buckling and free vibration laminated composite and sandwich beams: A critical review of literature. *Compos Struct*, 171:486–504.

Shakya, N. K. & Padhee, S. S. (2023). Asymptotic analysis of Timoshenko-like orthotropic beam with elliptical cross-section. *Eur J Mech A Solids*, 102:105100.

Sun, B. H. (2021). Geometry-induced rigidity in elastic torus from circular to oblique elliptic cross-section. *Int J Non-Linear Mech*, 135:103754.

Virgin, L. N., Santillan, S. T. & Holland, D. G. (2007). Effect of gravity on the vibration of vertical cantilevers. *Mech Res Commun*, 34:312–317.

Wang, C. Y. & Drachman, B. (1981). Stability of a heavy column with an end load. *J Appl Mech*, 48(3):668–669.

Yang, X. D., Zhang, X. D. & Chen, L. Q. (2013). Transverse vibration and stability of axially travelling sandwich beam with soft core. *J Vib Acoust*, 135:051013.